Geophysical Journal International

Geophys. J. Int. (2022) **229,** 2034–2046
Advance Access publication 2022 February 10
GJI Seismology

https://doi.org/10.1093/gji/ggac053

Bayesian differential moment tensor inversion: theory and application to the North Korea nuclear tests

Zhe Jia, Zhongwen Zhan and Donald Helmberger†

Seismological Laboratory, California Institute of Technology, Pasadena, CA 91125*, USA. E-mail: zjia@gps.caltech.edu*

Accepted 2022 February 7. Received 2022 January 19; in original form 2021 July 8

SUMMARY

Moment tensors are key to seismic discrimination but often require accurate Green's functions for estimation. This limits the regions, frequency bands and wave types in moment tensor inversions. In this study, we propose a differential moment tensor inversion (diffMT) method that uses relative measurements to remove the path effects shared by clustered events, thereby improving the accuracy of source parameters. Using results from regular inversions as *a priori* distribution, we apply Bayesian Markov Chain Monte Carlo to invert the body- and surface wave amplitude ratios of an event pair for refined moment tensors of both events. Applications to three North Korea nuclear tests from 2013 to 2016 demonstrate that diffMT reduces the uncertainties substantially compared with the traditional waveform-based moment tensor inversion. Our results suggest high percentages of explosive components with similar double-couple components for the North Korea nuclear tests.

Key words: Inverse theory; Earthquake monitoring and test-ban treaty verification; Earthquake source observations.

1 INTRODUCTION

Seismic moment tensor provides a point-source approximation of the radiation pattern and a measure of the event size. Different combinations of isotropic (ISO), double-couple (DC) and compensated linear vector dipole (CLVD) components can manifest the first-order physics of different event types, such as natural earthquakes, collapses, landslides and nuclear explosions, thus being used for their discrimination (Ford *et al.* 2009; Cesca *et al.* 2017; Alvizuri & Tape 2018). Furthermore, DC focal mechanisms provide important insights on regional stress state (Hauksson 1994; Hardebeck & Hauksson 2001; Wang & Zhan 2020b), plate interface morphology (Hayes *et al.* 2009; Zhan *et al.* 2012; Bazargani *et al.* 2013) and slab dynamics (Yang *et al.* 2017; Liu *et al.* 2021). In the past few decades, moment tensor inversion has gradually progressed from polarity-based to waveform-based inversion (Zhu & Helmberger 1996; Kanamori & Rivera 2008; Ekström *et al.* 2012). At the theoretical level, Tape & Tape (2012, 2013, 2015) proposed a mathematically intuitive way to view the moment tensors and examine the explosive and tensile mechanisms. Zhu & Ben-Zion (2013) developed a parametrization of full moment tensors with well-defined parameters for source inversion. These progresses in theory and inversion, together with the improving Earth structural modeling, reduce the focal mechanism errors to about 20° for most moderate to large events in the centroid moment tensor catalogues (Duputel *et al.* 2012).

However, accurate full moment tensor inversions for shallow sources are still challenging. Robust moment tensor solutions are usually only retrievable at long periods (e.g. $T > 20$ s; Minson & Dreger 2008) that are insensitive to small-scale structural heterogeneities. However, earthquakes and explosions of small to moderate size usually have limited near-field coverage and weak signals at long periods. For the short-period waves, modeling them is difficult because existing 3-D crustal velocity models are often inadequate in capturing small-scale heterogeneities at regional distances. Using inaccurate earth structural models could introduce errors in focal mechanisms and non-DC proportions (Frohlich & Davis 1999). Taking the North Korea nuclear explosions as an example, different studies show non-trivial differences of moment tensor solutions (Cesca *et al.* 2017; Alvizuri & Tape 2018; Chiang *et al.* 2018). For better azimuthal and take-off angle coverage, approaches that jointly invert regional and teleseismic waves have been proposed (Ni *et al.* 2010; Ford *et al.* 2012), but they still encounter difficulties from inaccurate Green's functions.

To accurately determine the moment tensors when the path structure is complex, approaches using 3-D Green's functions have been introduced (Covellone & Savage 2012; Wang & Zhan 2020a). Most models used to calculate the 3-D Green's function are traveltime- and waveform-based tomographic models. Traveltime tomographic models, such as the LLNL model by Simmons *et al.* (2012) and the SALSA3D model by Ballard *et al.* (2016), can predict body wave arrivals with significantly reduced errors than 1-D models, thereby

†Deceased on 2020 August 13

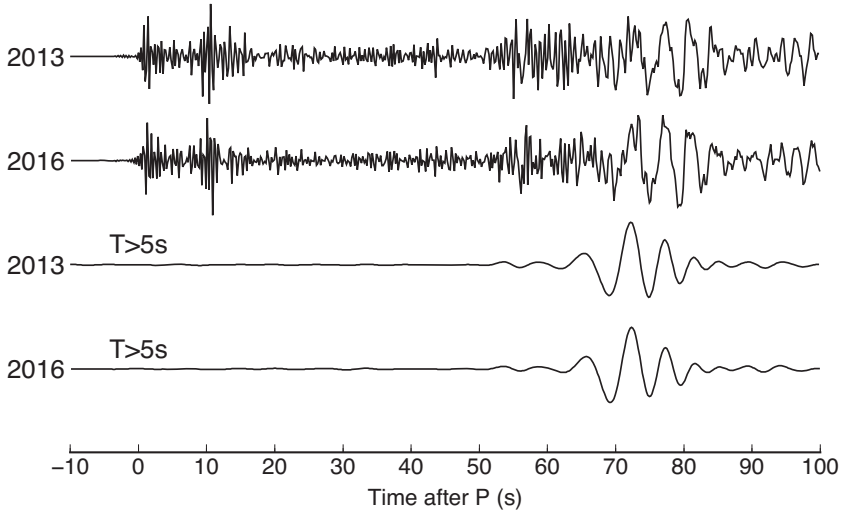

Figure 1. Waveform similarity of the February 2013 and January 2016 nuclear tests. The similarities in both broad-band (top two) and low-passed filtered (bottom two) waveforms recorded at station MDJ suggest shared path/site effects. Note that *P* waves are only visible at short periods. The epicentral distance is about 400 km.

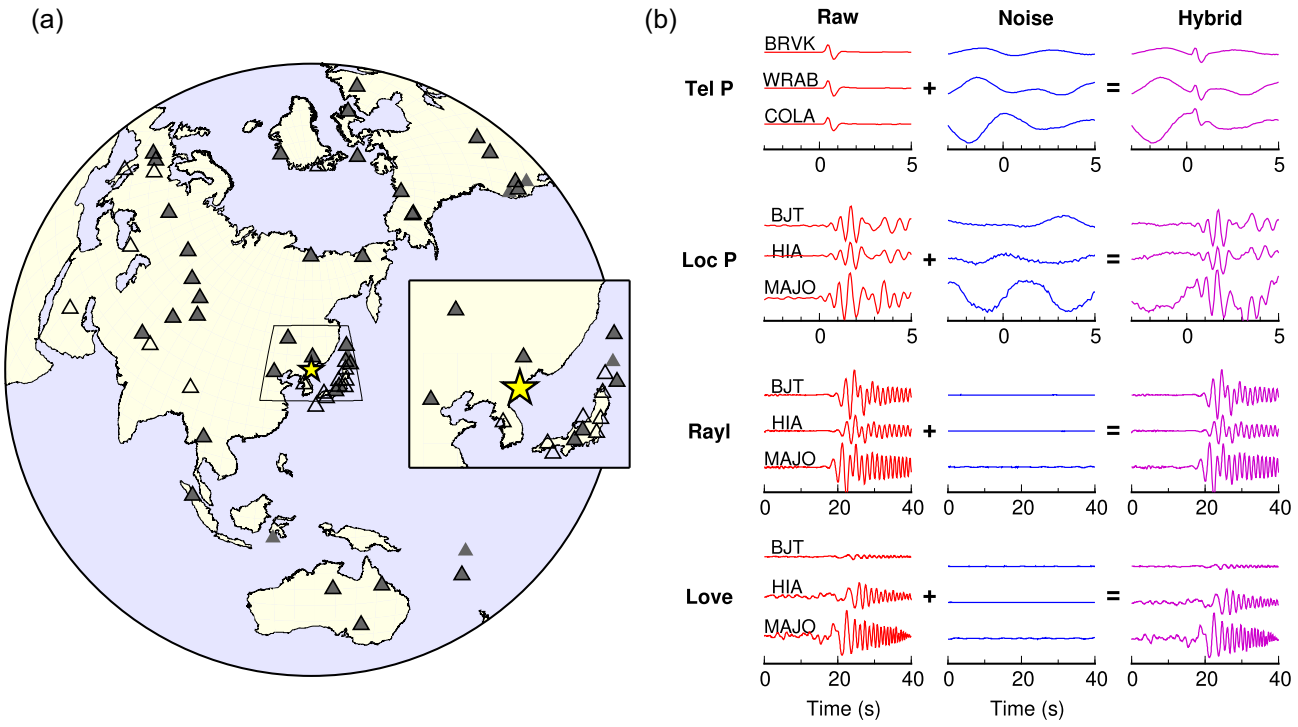

Figure 2. Generation of synthetic waveforms in our test. (a) Configuration of collocated sources (yellow star) and the seismic stations (grey triangles). Black-outlined triangles are the stations used in the following real-data inversions. The inset box shows the regional stations. (b) Adding real noise (blue lines) to the raw seismograms (red lines) for the hybrid synthetic data (purple lines).

being used to precisely detect and locate small seismic events. However, they are usually restricted by the smoothing in the inversions, and may not accurately fit the seismic waveforms. On the other hand, waveform-based tomographic models are more promising in explaining wiggles on seismograms (Fichtner *et al.* 2009; Tape *et al.* 2009; Bozdağ *et al.* 2016). However, most global and continental scale models use long-period waveforms (e.g. $T > 17$s globally) for inversion, due to the high computational cost. Only for specific areas of dense seismic monitoring, adjoint tomographic inversions based on higher frequency seismic waveforms have been developed and implemented in source inversions (Lee *et al.* 2014; Savage *et al.* 2014; Jia *et al.* 2020b).

To reduce the requirement of highly accurate velocity models, the empirical Green's function (EGF) methods are developed to study clustered explosions and earthquakes. Sites of artificial explosions are often clustered and share similar path and site effects. For example, all the North Korea nuclear tests were in the Punggye-ri site, within a few km from each other (Zhang & Wen 2013, 2015;

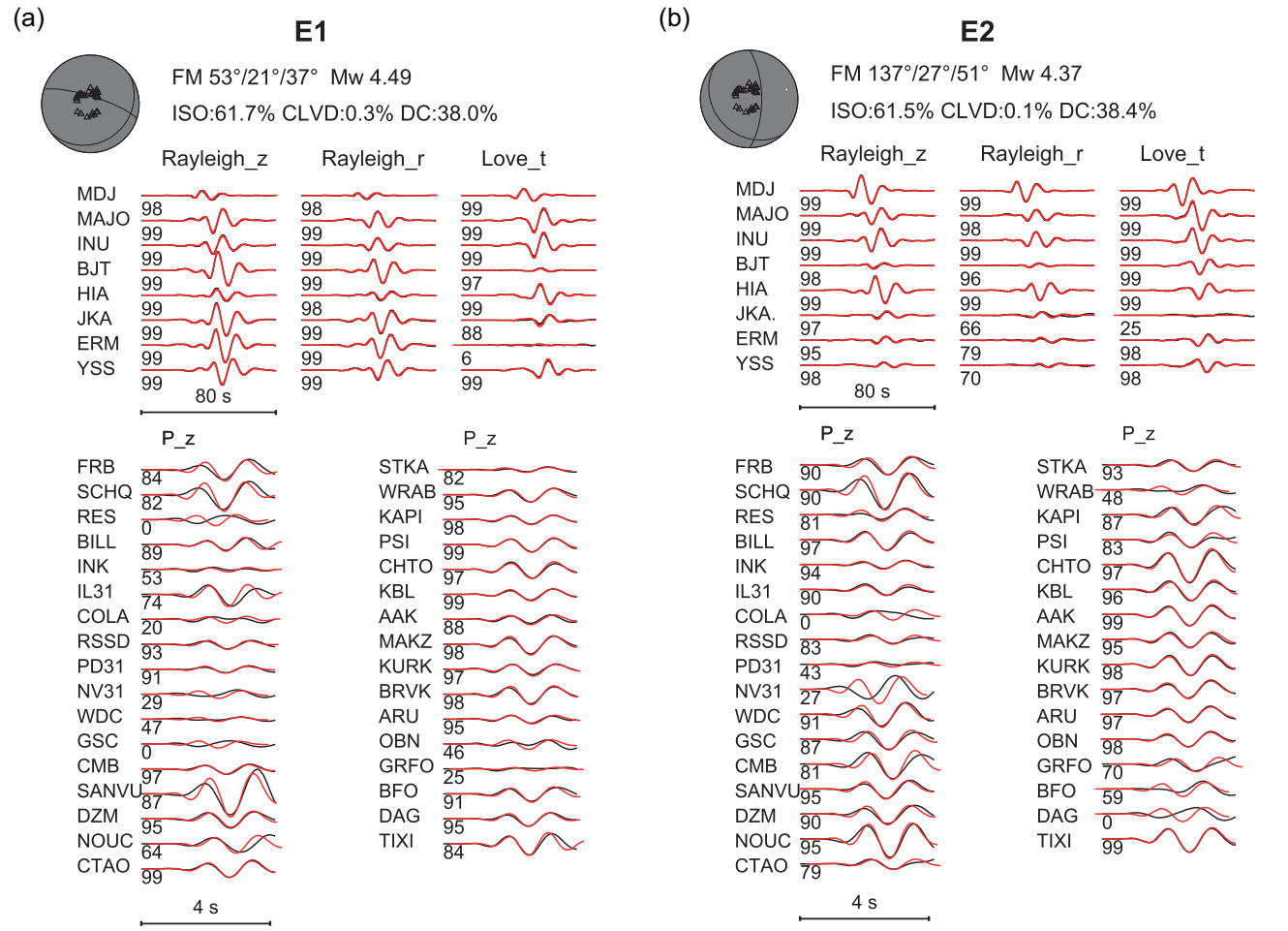

Figure 3. gCAP inversion results for the two synthetic events. The black and red lines indicate data and synthetic waveforms, respectively. The numbers leading the waveforms are the cross-correlation coefficients between data and synthetics.

Wang & Hutko 2018; Xu *et al.* 2020). As shown in Fig. 1, the regional waveforms from the February 2013 and January 2016 North Korea tests are highly similar at both broad-band and long periods ($T > 5$ s), suggesting overlapping paths and common station terms. This similarity makes nuclear tests ideal for EGF methods, which removes the structural terms using relative measurements. Ni *et al.* (2010) used tectonic earthquakes to calibrate the path and site effects, thereby improving the moment tensor inversions of nuclear tests. Lay *et al.* (1984) intercorrelated source time functions and waveforms of two nuclear events to remove path influences and determine their yield and depths, and the method has also been applied on the North Korean nuclear explosions (Voytan *et al.* 2019). For tectonic earthquakes, smaller EGF events can help investigate the mechanisms and ruptures of main shocks, including the 1994 Northridge earthquake (Dreger 1994) and the 2004 Sumatra earthquake (Vallée 2007).

Among the EGF approaches, relative moment tensor inversion methods stand out as a particular category. Similar to the double-difference relocation algorithm that removes common traveltime anomalies for more precise locations (Waldhauser & Ellsworth 2000), relative moment tensor inversions eliminate the path and site amplifications to reduce moment tensor errors. Plourde & Bostock (2019) used relative amplitudes of body waves among a cluster of seismic events to improve focal mechanisms. Such methods greatly reduce moment tensor errors, but they can also introduce bias by assuming the reference event is well resolved. Dahm (1996) avoided the assumption on a single reference event by using arbitrary *a priori* constraint, but facing the issues of interference bias and lack of uncertainty assessments. To better assess errors and to avoid arbitrary selection of reference events, we need to incorporate Bayesian statistics to the relative moment tensor inversion methods with appropriate *a priori* information.

In this study, we develop a differential moment tensor inversion (diffMT) algorithm to study paired seismic events in a Bayesian framework. We take amplitude ratios of various seismic phases to cancel out path and site effects, and expect reduced moment tensor errors. For nuclear tests, these should translate to better explosion discriminations and yield estimations. We verify the diffMT algorithm using synthetic data, and apply it to three North Korea nuclear tests between 2013 and 2016. We compare our results with traditional waveform inversion solutions and analyse the explosion and tectonic release components of these tests.

2 METHODS

Our diffMT method refines the waveform-based moment tensor prior distribution with additional differential measurements for an event pair. There are two steps. First, we apply the generalized Cut-and-Paste (gCAP) inversion for moment tensor solutions and their

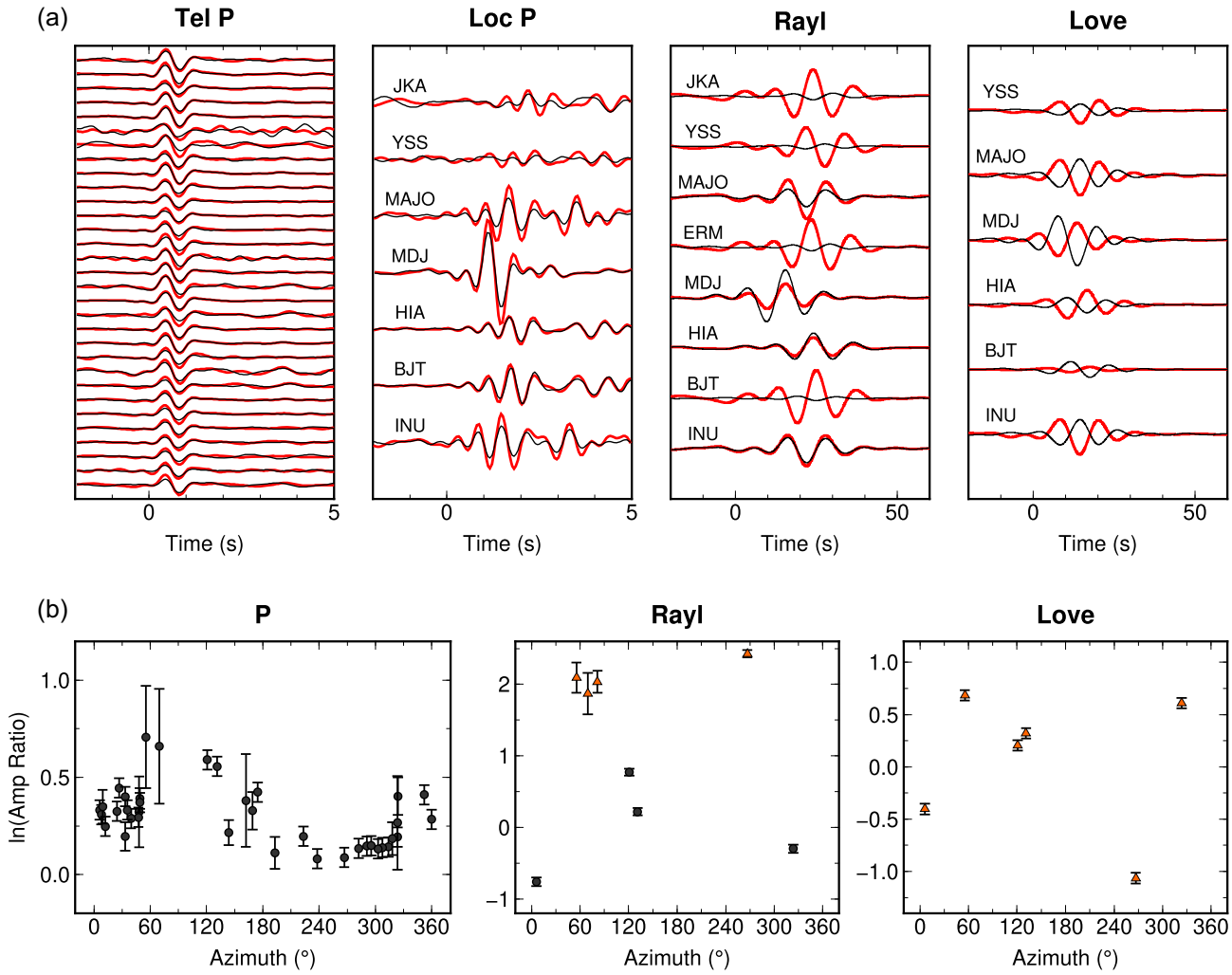

Figure 4. Measurement of amplitude ratios between two synthetic events. (a) Cross-correlated waveforms for teleseismic *P* (Tel P), regional *P* (Loc P), Rayleigh and Love waves, respectively. (b) Amplitude ratios for *P*, Rayleigh and Love waves as a function of the station azimuth. The Tel P and Loc P observations are plotted together. Black circles and orange triangles represent consistent and flipping polarities, respectively. The standard deviation errors are shown with the error bars.

uncertainties as the prior information. We then measure the amplitude ratios for regional and teleseismic *P* waves, regional Rayleigh and Love waves, and conduct Markov Chain Monte Carlo (MCMC) inversion on these differential measurements for the posterior distributions of moment tensor components.

2.1 Generalized Cut-and-Paste inversion for prior information

Our first step is equivalent to most traditional moment tensor inversions. In this study, we use gCAP (Zhu & Ben-Zion 2013) as our main driver for the waveform inversion, as improved by Bai *et al.* (2020) to combine near-field and teleseismic data. The CAP methodology (Zhao & Helmberger 1994; Zhu & Helmberger 1996) breaks seismograms into Pnl and S/Surface waves, and models them simultaneously but allows different time-shifts between observations and synthetics to accommodate inaccurate velocity models and earthquake locations. The generalized CAP (gCAP) method relieves the DC restriction for full moment tensor inversions. Here, we search for six independent parameters, including moment magnitude (M_w), ISO and CLVD components (ζ and χ), strike, dip and rake (Zhu & Ben-Zion 2013). The proportion of ISO (Λ^{ISO}), DC (Λ^{DC}) and CLVD (Λ^{CLVD}) components are represented by

$$\Lambda^{ISO} = \zeta^2, \tag{1}$$

$$\Lambda^{DC} = \left(1-\zeta^2\right) * \left(1-\chi^2\right), \tag{2}$$

$$\Lambda^{CLVD} = \left(1-\zeta^2\right) * \chi^2. \tag{3}$$

We use the bootstrapping resampling approach (Zhan *et al.* 2012; Jia *et al.* 2017) to estimate the source parameter uncertainties, which is used as *a priori* constraint for the following Bayesian MCMC inversions. Calculations of Green's functions are based on the propagator matrix method with plane wave approximation (Kikuchi & Kanamori 1991) for the teleseismic body waves, and the frequency–wavenumber integration method (Zhu & Rivera 2002) for regional surface waves.

2.2 Prediction and measurement of amplitude ratios

We calculate amplitude ratios of regional *Pn*/*P*, teleseismic *P*, regional Rayleigh and Love waves from two events to cancel out the

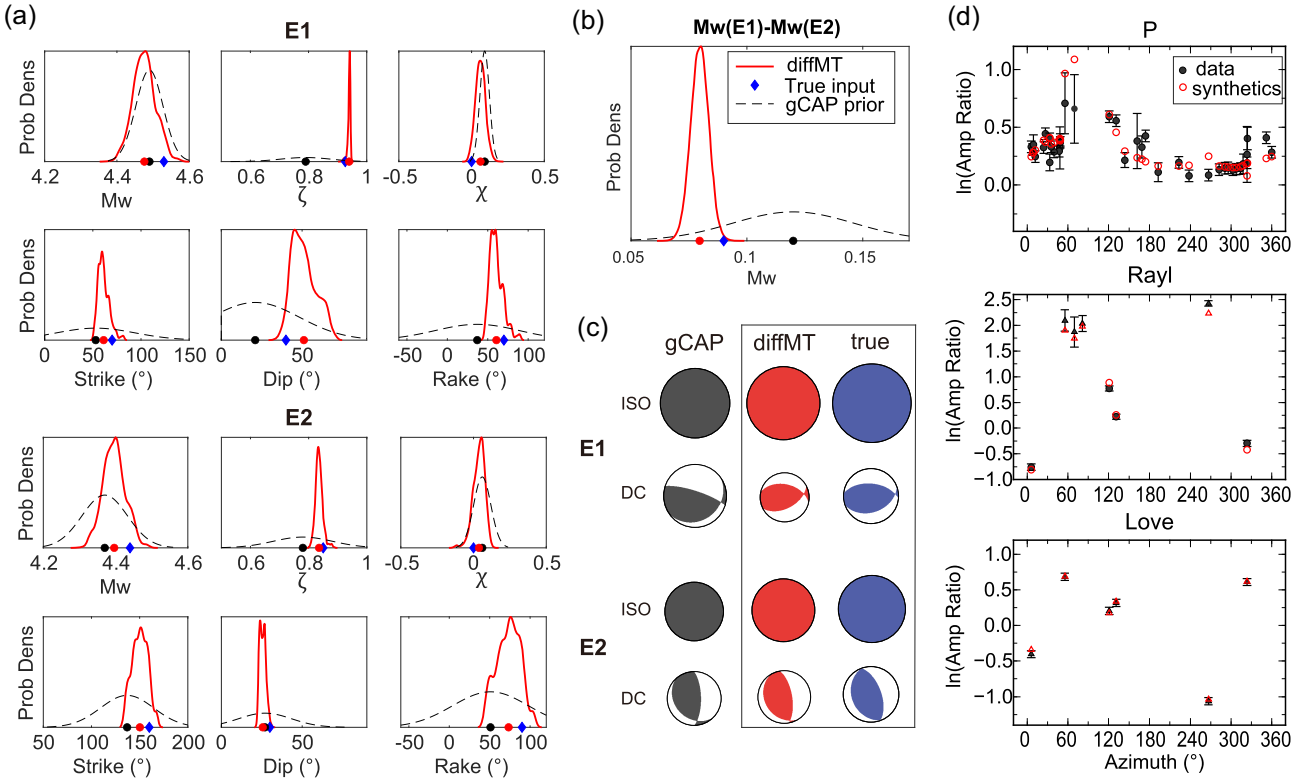

Figure 5. DiffMT inversion results for the two synthetic events. (a) The gCAP prior (dashed black lines) and the diffMT posterior (red lines) PDFs of the moment tensor solutions of the two events. The prior (gCAP) is from Gaussian fitting of bootstrapping uncertainties. Black and red dots indicate the gCAP optimal solution and mean of the diffMT posterior distribution, respectively. Blue diamond represents the true input value. See legend in (b). (b) The prior (dashed black lines) and posterior (red lines) PDFs of the moment magnitude difference between E1 and E2. Symbols are similar to that in (a). (c) Comparison of the isotropic (ISO) and double couple (DC) focal mechanisms for the gCAP (black) and diffMT (red) solutions. Blue beach balls show the true focal mechanisms. The sizes of beach balls are proportional to the corresponding magnitudes. (d) Amplitude ratio fittings for the diffMT solution. Black squares and red symbols show the amplitude ratio data and predictions from the moment tensor models, respectively. Circles and triangles represent consistent and flipping polarities, respectively.

path and site effects. The far-field seismic waves of an event pair can be represented by

$$u_1\ (\boldsymbol{x},t) = M_{ij}^1 * G_{ij}\,(\boldsymbol{x},t) * S_1\,(t) * r\,(\boldsymbol{x})\,, \tag{4}$$

$$u_2\ (\boldsymbol{x},t) = M_{ij}^2 * G_{ij}\,(\boldsymbol{x},t) * S_2\,(t) * r\,(\boldsymbol{x})\,, \tag{5}$$

where M_{ij} is the full moment tensor, G_{ij} is the Green's function, S is the source time function and r is the station amplification term. If we use body waves at periods longer than the source durations, we can reasonably approximate the studied events as point sources, and remove common path/site effects by taking amplitude ratios. For regional and teleseismic P waves recorded at the same station, the amplitude ratios of point sources are equivalent to their radiation pattern ratios, which is a function of take-off angle and azimuth, based on ray theory being implemented in a layered elastic media (Dahm 1996).

On the other hand, the surface wave amplitude ratios are complex functions of the moment tensors and depths. When the source depth h is much less than the wavelength as in the case of nuclear tests, certain surface wave eigenfunction terms are reduced to 0,

$$l_2\ (h) = \mu \frac{\mathrm{d}l_1}{\mathrm{d}z}|_h\ =\ 0, \tag{6}$$

$$r_3\ (h) = \mu \left(\frac{\mathrm{d}l_1}{\mathrm{d}z} - kr_2\right)|_h\ =\ 0, \tag{7}$$

$$r_4\ (h) =\ 0, \tag{8}$$

where r and l are components of the Rayleigh and Love wave motion-stress vectors, and the excitation of Rayleigh and Love waves is given by

$$\boldsymbol{u}^{\mathrm{Rayl}}\,(\boldsymbol{x},\omega)\ =\boldsymbol{G}^{\boldsymbol{R}}\ [U_1 + U_2\cos 2\phi + U_3 \sin 2\phi]\,, \tag{9}$$

$$\boldsymbol{u}^{\mathrm{Love}}\,(\boldsymbol{x},\omega)\ =\boldsymbol{G}^{\boldsymbol{L}}\ [U_2\sin 2\phi - U_3 \cos 2\phi]\,, \tag{10}$$

where $\boldsymbol{G}^{\boldsymbol{R}}$ and $\boldsymbol{G}^{\boldsymbol{L}}$ are given by

$$\boldsymbol{G}^{\boldsymbol{R}}\,(\boldsymbol{x};h,\omega)\ = \sum_n \frac{k_n r_1\,(h)}{8cUI_1}\sqrt{\frac{2}{\pi k_n r}}\exp\left[i\left(k_n r + \frac{\pi}{4}\right)\right][r_1\,(z)\,\hat{\boldsymbol{r}} + ir_2\,(z)\,\hat{\boldsymbol{z}}]\,, \tag{11}$$

$$\boldsymbol{G}^{\boldsymbol{L}}\,(\boldsymbol{x};h,\omega)\ = \sum_n \frac{ik_n l_1\,(h)}{8cUI_1}\sqrt{\frac{2}{\pi k_n r}}\exp\left[i\left(k_n r + \frac{\pi}{4}\right)\right] l_1\,(z)\,\hat{\phi}, \tag{12}$$

in which μ is the shear modulus, r is the distance, z is the depth, $\hat{\boldsymbol{r}}$, $\hat{\boldsymbol{z}}$, ϕ are the unit vectors for three cylindrical coordinates and k_n is the nth root of the wave number (Aki & Richards 2002). The radiation pattern coefficients U_1, U_2, U_3 are given by

$$U_1 = \frac{1}{2}\ \left(\boldsymbol{M}_{xx} + \boldsymbol{M}_{yy}\right) - \left(1 - \frac{2\beta^2}{\alpha^2}\right)\boldsymbol{M}_{zz}, \tag{13}$$

$$U_2 = \frac{1}{2}\ \left(\boldsymbol{M}_{xx} - \boldsymbol{M}_{yy}\right), \tag{14}$$

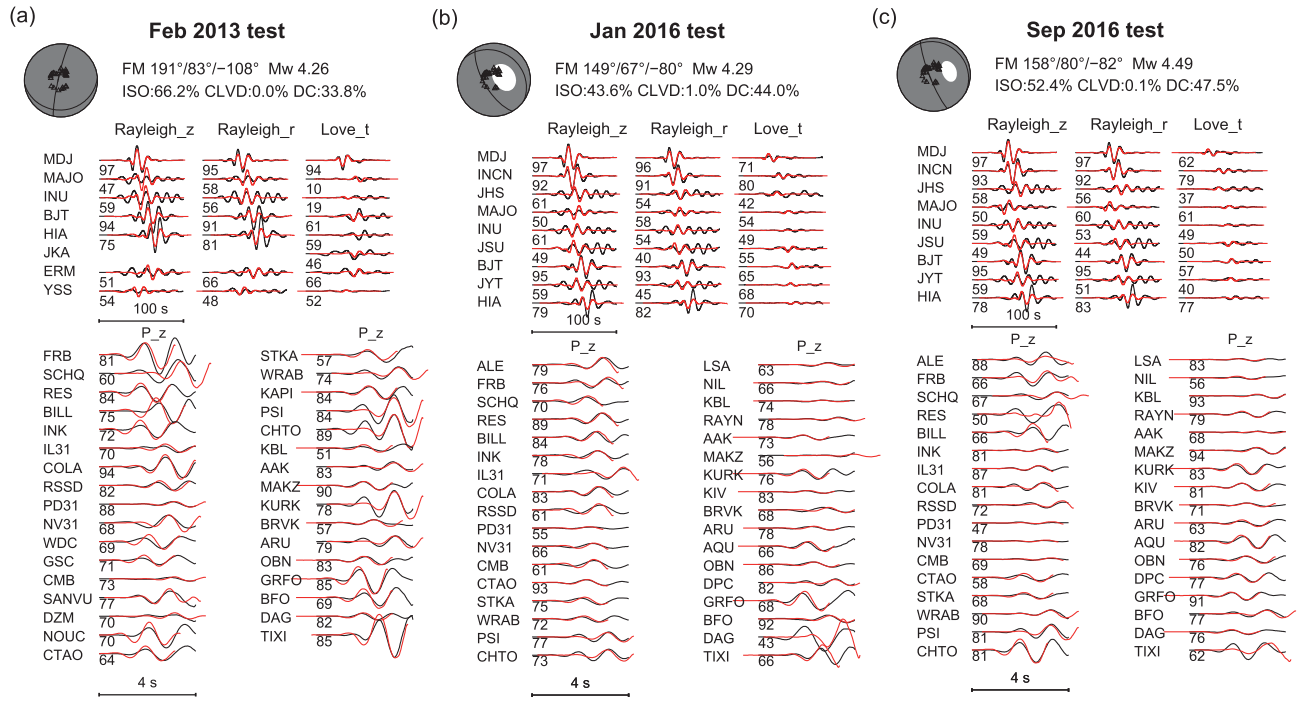

Figure 6. gCAP inversion results for the three studied North Korea nuclear explosions on (a) February 2013, (b) January 2016 and (c) September 2016, respectively. The symbols are similar to that in Fig. 3.

$$U_3 = \boldsymbol{M}_{xy} \,. \tag{15}$$

When two events E1 and E2 are both shallow and closely located, they share similar $\boldsymbol{G^R}$ and $\boldsymbol{G^L}$. Hence these terms can be cancelled out by calculating the amplitude ratios. The analytical form of Rayleigh and Love wave amplitude ratios would be functions of moment tensors $\boldsymbol{M}_{E1}$, $\boldsymbol{M}_{E2}$, Vp/Vs ratios β/α and station azimuth ϕ,

$$\boldsymbol{A^R}|_{\frac{E1}{E2}} = \frac{(U_1 + U_2\cos 2\phi + U_3 \sin 2\phi)\,|_{E1}}{(U_1 + U_2\cos 2\phi + U_3 \sin 2\phi)|_{E2}} \,, \tag{16}$$

$$\boldsymbol{A^L}|_{\frac{E1}{E2}} = \frac{(U_2\sin 2\phi - U_3 \cos 2\phi)|_{E1}}{(U_2\sin 2\phi - U_3 \cos 2\phi)|_{E2}} \,, \tag{17}$$

This means we can also take the path effects away by calculating amplitude ratios of surface waves.

For vertical component *P* waves, we cut 3-s time windows right after the hand-picked *P* arrivals, and cross-correlate to measure the amplitude ratios. We calculate two different terms,

$$A^1 = \frac{\int \boldsymbol{u}\,(\tau - t)\,\boldsymbol{v}\,(\tau)\,\mathrm{d}\tau}{\int \boldsymbol{v}^2\,(\tau)\,\mathrm{d}\tau}, \tag{18}$$

$$A^2 = \frac{\int \boldsymbol{u}^2\,(\tau)\,\mathrm{d}\tau}{\int \boldsymbol{u}\,(\tau - t)\,\boldsymbol{v}\,(\tau)\,\mathrm{d}\tau}, \tag{19}$$

where $\boldsymbol{u}(t)$ and $\boldsymbol{v}(t)$ are the wave segments of two events after cross-correlation. The terms A^1 and A^2 are similar to the waveform-coherency-based amplitude ratio defined in an adjoint tomographic inversion (Tao *et al.* 2017) and reflect the waveform similarity of the cross-correlations. The term A^1 generally represents $\boldsymbol{u}/\boldsymbol{v}$, while A^2 represents $1/(\boldsymbol{v}/\boldsymbol{u})$ after an appropriate time-shift. If $\boldsymbol{u}$ and $\boldsymbol{v}$ have the same waveform shape (correlation coefficient = 1), A^1 and A^2 would be identical and equal to the amplitude amplification factor (AAF; Tan & Helmberger 2007). Otherwise, A^1 will be smaller and A^2 will be larger than the AAF. Therefore, it is logical to take A^1 and A^2 as lower and upper bounds to assess the waveform-coherency-dependent amplitude ratio variations. We take the natural logarithm of the absolute values of A^1 and A^2, and choose their mean as data and the half deviation as data uncertainty. Besides, we extract the polarity difference from cross-correlations as part of the differential data. We use 1 and −1 to represent the same and opposite polarities of the event pair at each station, and use their difference (2) as 3 times standard deviation error (99% confidence limit).

Measurement of the Rayleigh and Love wave amplitude ratios and errors is similar to that of body waves. We choose the time window to be 60s centred at the peak envelope amplitudes for cross-correlations. Specifically for Rayleigh waves, we take the largest deviation between $\ln(|A^1|)$ and $\ln(|A^2|)$ for both radial and vertical components for the amplitude ratio errors.

2.3 Bayesian Markov Chain Monte Carlo inversion

We use the Metropolis–Hasting Markov Chain Monte Carlo (MCMC) method to estimate the posterior probability density functions (PDFs) by fitting the differential measurements (i.e. amplitude ratios and polarity differences) of body and surface waves. The MCMC inversion follows a Bayesian framework, which produces model distribution from data fittings and the *a priori* information (Tarantola 2005),

$$p(\boldsymbol{m}|\boldsymbol{d}) \propto p\,(\boldsymbol{m}) * l(\boldsymbol{d}|\boldsymbol{m}), \tag{18}$$

where the $p(\boldsymbol{m})$ and $p(\boldsymbol{m}|\boldsymbol{d})$ are prior and posterior PDFs, respectively. d indicates the amplitude ratio data, including logarithmic amplitude ratios and polarity differences. m represents the six independent source parameters (M_w, ζ, χ, strike, dip and rake) for each event, in total 12 parameters for an event pair. Conversion from the data to model is performed through the likelihood function, which describes how the predictions from a model fit the data within data

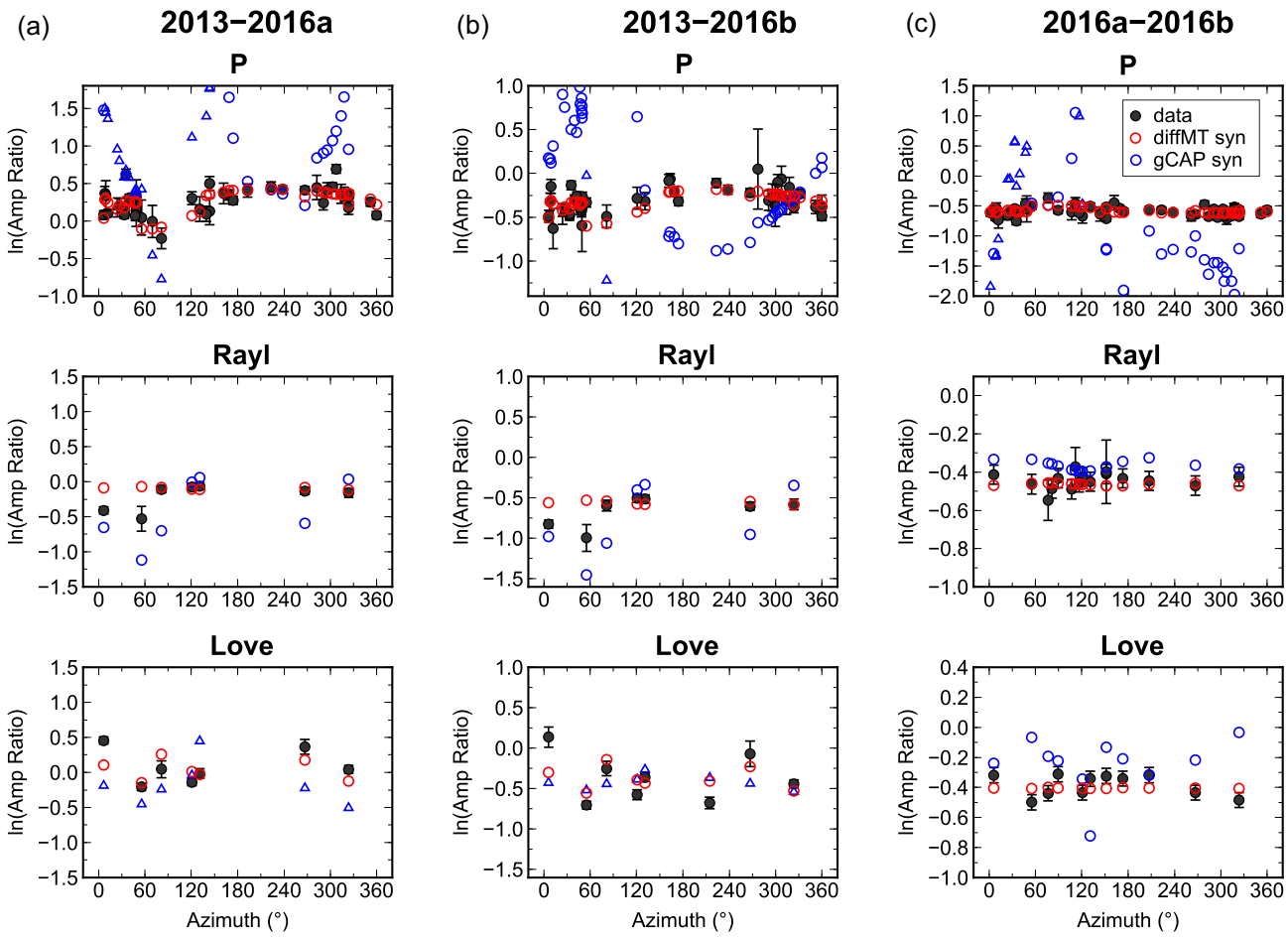

Figure 7. Amplitude ratios among the February 2013, January 2016 (2016a) and September 2016 (2016b) events. Three pairs are shown in (a)-(c), respectively. Circles and triangles represent consistent and flipping polarities, respectively. Black symbols with error bars show the amplitude ratio measurements. Blue and red symbols indicate the amplitude ratio predictions from the gCAP and diffMT solutions, respectively.

error. Our likelihood function is defined as the following equation,

$$l\,(\boldsymbol{d}|\boldsymbol{m}) = \frac{1}{\sqrt{(2\pi)^N\,|\boldsymbol{C_d}|}}\,\exp\left(-\frac{1}{2}(G\,(\boldsymbol{m})-\boldsymbol{d})^T\boldsymbol{C_d}^{-1}\,(G\,(\boldsymbol{m})-\boldsymbol{d})\right), \qquad (19)$$

where G is the forward simulation operator, and $\boldsymbol{C_d}$ is the data covariance matrix. We assume that $\boldsymbol{C_d}$ is diagonal:

$$\boldsymbol{C_d}_{ii} = \sigma_i^2\,,\quad i \in [1,\ N]\,, \qquad (20)$$

$$\boldsymbol{C_d}_{(i+N)(i+N)} = \varepsilon_i^2\,,\quad i \in [1,\ N]\,, \qquad (21)$$

where σ_i and ε_i are the standard deviation errors of logarithmic amplitude ratio and polarity difference at the ith station, respectively. To avoid the inversion being dominated by data points of minimal errors, we set σ_i to be no less than 0.05, corresponding to ∼5% amplitude ratio difference. Here we assumed no correlation between data errors for different stations, different phases, and various measurement types (amplitude ratios versus polarities), which may not best reflect the true covariance. But because the P and surface waves are well separated, and Rayleigh and Love waves have orthogonal direction of vibration, their interferences are unlikely substantial. It's also reasonable to ignore the covariance between amplitude ratios and polarities, as they would be correlated only when the observation is close to the nodal, which is the minority of all stations.

We use Markov Chain Monte Carlo (MCMC) method to sample the posterior PDF $p(m|d)$. For low-dimension problems, brutal force algorithms are sufficient to sample the posterior PDF. When the dimensionality increases (e.g. >10), the volume of the model space increases exponentially, and the available trials become too sparse to grid-search the models. Instead, MCMC allows us to sample higher dimension distributions of known form but difficult to grid-search. Guided by the form of the posterior PDF, a Markov Chain randomly walks through the model space and results in an ensemble of models which density follows the target distribution. The models move to higher posterior probabilities with Gaussian random perturbations, and can still accept less likely models and thus jumping out of the local minimums (Hastings 1970).

We generate 200 Markov Chains, and eventually keep 1/4 chains with highest posterior probability to avoid being trapped in low posterior minima. For each chain, we randomly generate 200 samples, and select the one of highest posterior probability as the initial draw. We apply the Gaussian proposal distributions to perturb the model at each step towards a new model. The Gaussian proposal distribution of each parameter has a standard deviation of 1/10 standard deviation of its prior distribution. We follow the Metropolis Hasting algorithm (Hastings 1970) to drive the random walk, but different from conventional Metropolis–Hasting algorithm which perturb all parameters simultaneously, we propose new models by sampling one parameter while keeping the other parameters at their current

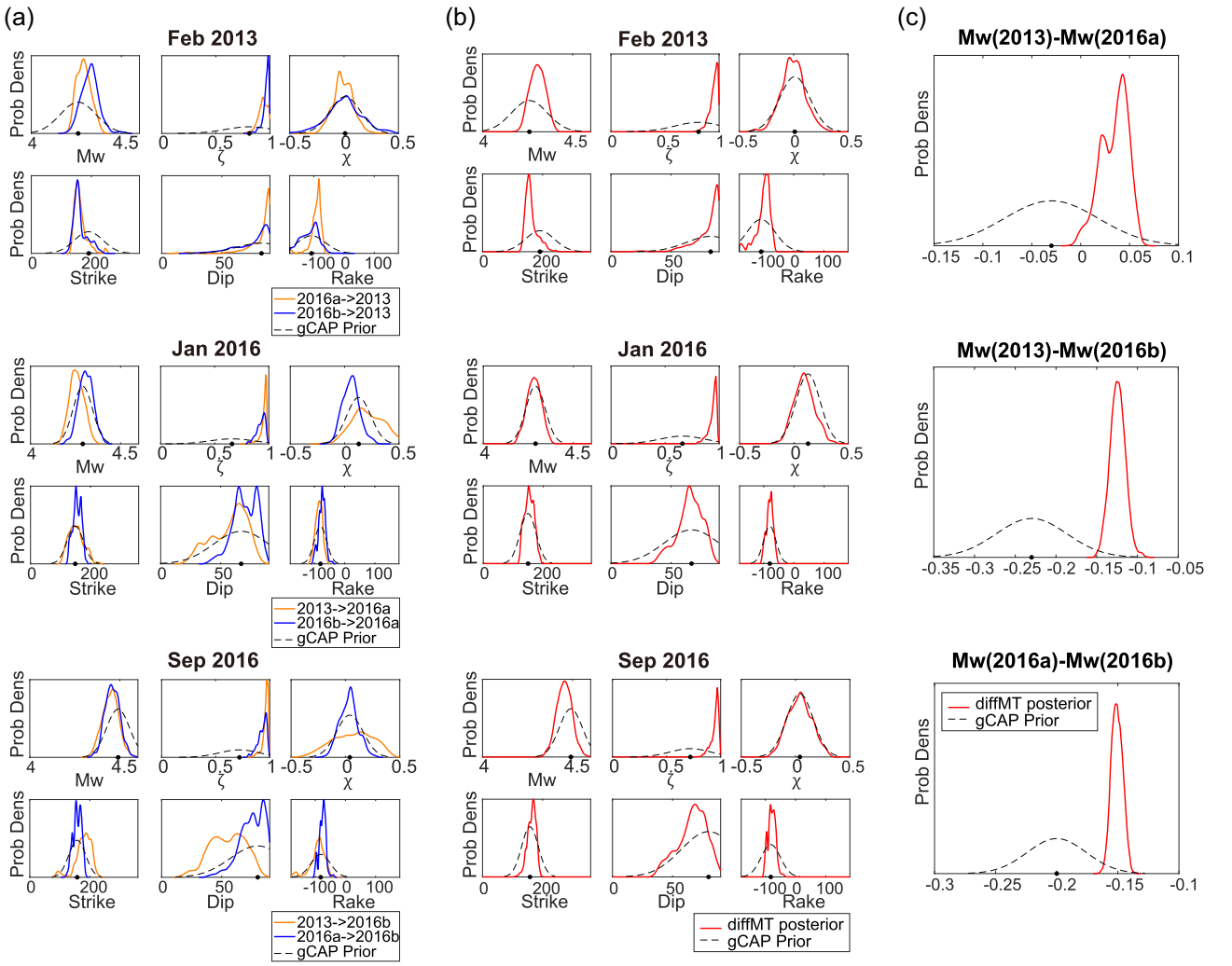

Figure 8. DiffMT inversion results for the event pair of the February 2013 and January 2016 tests. (a) The gCAP prior (dashed black lines) and the diffMT posterior (solid lines) PDFs of the moment tensor solutions of the two events. Solid lines in different colours indicate the posterior PDFs derived with different pairing events. Black dots show the optimal gCAP solution. (b) Combined posterior PDFs (solid red lines) plotted with the gCAP prior PDFs (dashed black lines). (c) The prior (dashed black lines) and posterior (red lines) PDFs of the moment magnitude differences.

values (Jia *et al.* 2020a). The parameter being perturbed is randomly selected. This approach ensures a high acceptance rate and improves the efficiency of convergence. Our Markov Chains usually converge in hundreds to thousands of iterations, but we choose a conservative number of burn-in samples to be 20 000. After the burn-in stage, we keep the next 20 000 samples in each chain, and combine 50 chains to form the final ensemble for the posterior PDFs.

3 SYNTHETIC TEST

We first benchmarked diffMT with synthetics, using the configuration of two collocated nuclear tests at the North Korea test site. Nuclear events have shallow burial depths and short duration, thus fitting our assumptions well. We put the pair at depths of 0.6 km, and with the E1 moment tensor as (M_w 4.53, Λ^{ISO}= 86%, strike/dip/rake = 70°/40°/70°) and the E2 moment tensor as (M_w 4.44, Λ^{ISO}= 73%, strike/dip/rake = 160°/30°/90°). Using these source parameters, we calculated synthetic seismograms for 8 regional (within epicentral distance of 15°) and 33 teleseismic (epicentral distance between 30° and 90°) stations (Fig. 2a). The velocity model used is based on a combination of a three-layer 1-D elastic model (Ford *et al.* 2009) and the iasp91 model (Kennett *et al.* 1995). We collected real seismic noise for the used stations, and added them to the synthetic waveforms (Fig. 2b) for a similar level of signal-to-noise ratio (SNR) as natural nuclear test events. After adding the noise, the synthetic surface waves still have high SNRs, while the body waves are generally hard to observe in broadband. This is similar to the real data for most North Korea nuclear tests.

We first applied the gCAP inversion on the two events. We filtered the data and synthetics between 0.03–0.1 Hz for regional surface waves and 0.5–1.0 Hz for teleseismic body waves. Modelling the real site amplifications of high-frequency *P* waves is difficult, so we normalized the *P* waves data to the synthetic wave amplitudes and only fit the waveform shapes. We also fixed the source depths to 0.6 km, approximated from Voytan *et al.* (2019), due to the limited data resolution. The moment tensor results have ∼60% ISO components for both E1 and E2 (Fig. 3), which is smaller than the input model. Moreover, the DC focal mechanisms deviate ∼30 degrees from the input values. We estimated the moment tensor standard deviation errors using 200 bootstrapping resamples, and

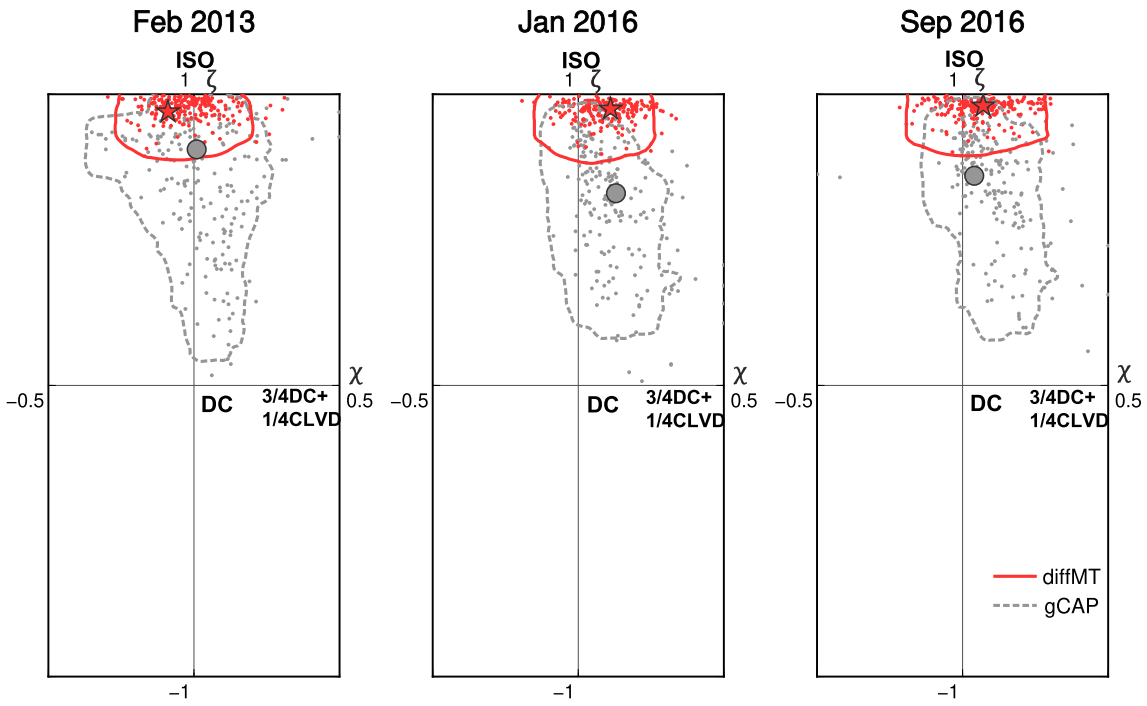

Figure 9. Prior (gCAP) and posterior (diffMT) distributions of ζ and χ for the three studied events. Red star and grey circle indicate diffMT and gCAP solution, respectively. The diffMT samples (red scattered dots) are contoured by the 90% confidence limit lines (red solid line), while the grey scattered dots and dashed lines are the gCAP samples and 90% confidence limits.

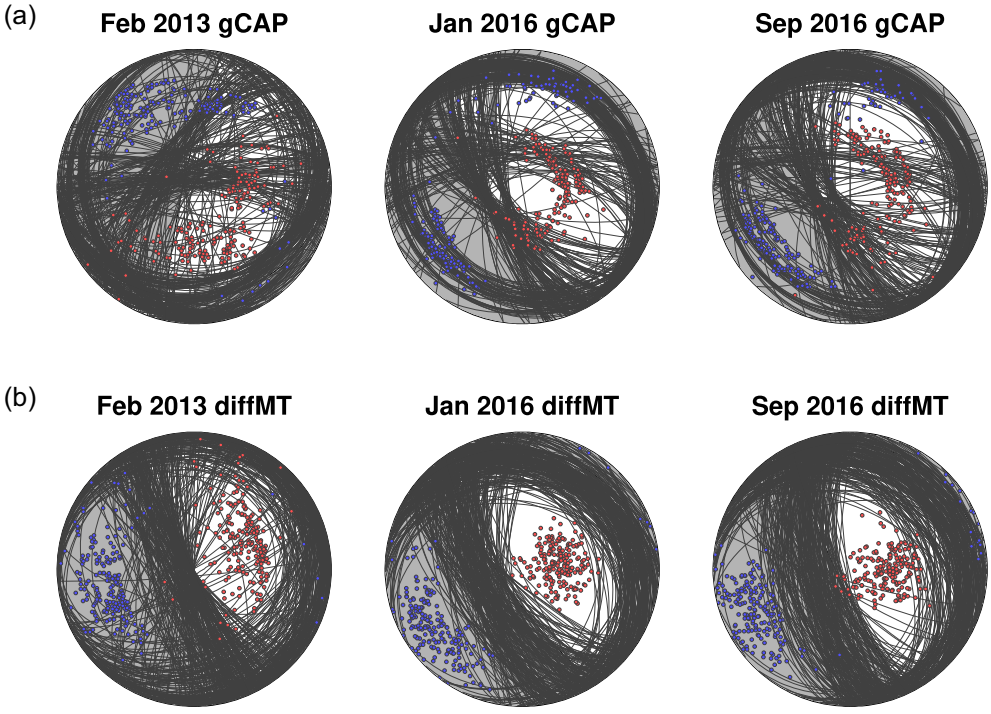

Figure 10. Scatter plot of the focal mechanisms from the (a) gCAP prior and (b) diffMT posterior ensembles. Red and blue dots are the P and T axes of the focal mechanisms, respectively.

observed substantial uncertainties for both E1 and E2 (Supporting Information Fig. S1). Given the minor data misfits (Fig. 3), the non-trivial moment tensor errors reflect poor data constraints due to limited frequency band and sparse network.

After obtaining the gCAP solutions and uncertainties, we converted them to Gaussian *a priori* information for the diffMT inversion. We measured the amplitude ratios of regional and teleseismic *P* waves, and regional Rayleigh and Love waves. We filtered the

Table 1. Moment tensor solutions for the 3 studied North Korea nuclear tests.

	M_w	ζ	χ	Strike (°)	Dip (°)	Rake (°)	Λ^{ISO}(per cent)	Λ^{DC}(per cent)	Λ^{CLVD}(per cent)
Feb 2013 (prior)	$4.26^{+0.20}_{-0.20}$	$0.81^{+0.19}_{-0.44}$	$0.01^{+0.14}_{-0.14}$	191^{+96}_{-96}	83^{+7}_{-40}	-108^{+94}_{-72}	66^{+34}_{-50}	34^{+50}_{-34}	0^{+2}_{-0}
Feb 2013 (diffMT)	$4.31^{+0.06}_{-0.07}$	$0.94^{+0.06}_{-0.07}$	$-0.09^{+0.27}_{-0.1}$	154^{+51}_{-17}	79^{+10}_{-22}	-92^{+21}_{-58}	88^{+12}_{-12}	12^{+11}_{-11}	0^{+1}_{-0}
Jan 2016 (prior)	$4.29^{+0.10}_{-0.10}$	$0.66^{+0.34}_{-0.40}$	$0.13^{+0.22}_{-0.22}$	149^{+53}_{-53}	67^{+23}_{-46}	-80^{+41}_{-41}	44^{+56}_{-37}	56^{+27}_{-43}	0^{+8}_{-0}
Jan 2016 (diffMT)	$4.28^{+0.07}_{-0.07}$	$0.95^{+0.03}_{-0.09}$	$0.11^{+0.15}_{-0.17}$	161^{+18}_{-33}	61^{+20}_{-16}	-90^{+28}_{-10}	91^{+5}_{-17}	9^{+17}_{-6}	0^{+1}_{-0}
Sep 2016 (prior)	$4.49^{+0.13}_{-0.13}$	$0.72^{+0.28}_{-0.37}$	$0.04^{+0.24}_{-0.24}$	158^{+56}_{-56}	80^{+10}_{-46}	-82^{+64}_{-64}	52^{+48}_{-40}	48^{+40}_{-42}	0^{+6}_{-0}
Sep 2016 (diffMT)	$4.43^{+0.09}_{-0.05}$	$0.96^{+0.03}_{-0.09}$	$0.07^{+0.16}_{-0.21}$	163^{+21}_{-25}	66^{+18}_{-23}	-89^{+30}_{-10}	92^{+6}_{-16}	8^{+16}_{-6}	0^{+1}_{-0}

surface waves between 0.03–0.1 Hz, consistent with the gCAP inversion. For the *P* waves, we applied 0.5–2.0 Hz filter band for higher SNRs. Most waveforms of the two events show high similarity, with polarity flips for some surface wave components (Fig. 4a). The amplitude ratios show clear azimuthal variations (Fig. 4b), which are presumably caused by the radiation pattern difference of the two events.

With the amplitude ratio data derived from absolute amplitudes, we conducted diffMT inversion using MCMC sampling. The inversion results and data fittings are shown in Fig. 5. The posterior probability density functions (PDFs) are significantly narrower than the prior PDFs, showing reduced moment tensor uncertainties (Fig. 5a). The optimal source parameters from diffMT inversion are also closer to the true input values, and the moment magnitude difference is 0.08, closer to the true difference (0.09) than the prior difference (0.12) (Fig. 5b). The 3-D rotation angle between diffMT (61°/51°/61°) and true solution of E1 is 13°, significantly less than the 27° rotation between the gCAP and true solution (Fig. 5c). Similar improvement is observed for E2, where the 3-D rotation angle between diffMT (150°/26°/73°) and the true solution is 10°, less than the rotation angle between the gCAP and true solution (22°) (Fig. 5c). This is primarily because the azimuthal variations of the amplitude ratios, which is well fit by the diffMT synthetics (Fig. 5d), provide additional constraints that improve the moment tensor accuracy.

4 APPLICATION ON NORTH KOREA NUCLEAR TESTS

We applied our diffMT algorithm to the three North Korea nuclear tests on February 2013, January 2016 and September 2016, respectively, by conducting inversions on three event pairs using seismograms from regional (within epicentral distance of 15°) and teleseismic (epicentral distance between 30° and 90°) stations (Fig. 3). The numbers of observations for all three events are not identical due to the varying station availability across the time period, but since the overlapping stations are the majority, the azimuthal and distance coverage differences are trivial. Similar to the synthetic test, we first run gCAP inversion using the regional surface waves in velocity filtered between 0.03–0.1 Hz, and the teleseismic *P* waves in velocity filtered between 0.5–1.0 Hz. The narrow *P* wave filter band is a compromise between signal observability and modelling capability. We fixed the depths to be 0.6 km, similar to the estimations from Voytan *et al.* (2019), to avoid depth ambiguities. The inversion results show that both the regional and teleseismic waveforms are fit well (Fig. 6). We observe 50–70% ISO component for these events, which is generally consistent with other moment tensor inversion studies (Ford *et al.* 2009; Cesca *et al.* 2017; Chiang *et al.* 2018). The distributions of the moment tensors estimated from the bootstrapping resampling suggest that all the source parameter components have large uncertainties (Supporting Information Fig. S2). Particularly, the ISO component fraction and DC orientations are not well constrained. The wide range of model uncertainties makes it difficult to discriminate the explosions or to analyse the tectonic release mechanisms.

We measure amplitude ratios of the three event pairs among these three tests, using regional and teleseismic *P* waves between 0.5 and 2.0 Hz, and the Rayleigh and Love waves between 0.03 and 0.1 Hz. Waveforms of different events show high similarity, indicating robust measurements of the amplitude ratios (Supporting Information Fig. S3). The amplitude ratios have moderate azimuthal variation patterns (Fig. 7), which suggests different DC mechanisms under the dominant ISO components.

We further applied three separate diffMT inversions on these pairs. We did not choose doing one inversion for all events, due to the rapidly growing number of unknowns (N∗6) for N events, which would pose a significant challenge to the nonlinear searching efficiency. Conducting multiple paired inversions would be the most applicable way of diffMT application on the real-world seismic event clusters. To avoid the inversion being trapped to pure ISO sources ($\zeta = 1$) which generates very low Love wave amplitudes and numerically unstable ratios, we tapered the prior of ζ (eq. 1) from its maximum bootstrapping value (0.98/0.96/0.96 for the February 2013, January 2016 and September 2016 events) to 1. The existence of Love waves also does not support pure ISO source mechanisms. The diffMT posterior probability density functions (PDFs) are shown in Fig. 8. The posterior PDFs for each event are generally consistent from different pairs (Fig. 8a). Still, we can observe mismatches for some components, such as the rake angle for the February 2013 event, and CLVD parameter for the two 2016 tests (Fig. 8a). This is because models that fit amplitude ratio data for different pairs can have different biases from varying data errors. As long as they have overlapping model space, they do not contradict each other since the overlapped models could fit the data for both pairs. On the other hand, the CLVD factor χ may not be well constrained, because the CLVD component is a minor term accompanied with the DC mechanism (Zhu & Ben Zion 2013), while the DC part is already second order compared to the dominant ISO mechanism.

We multiplied the diffMT posterior PDFs of each event from different pairs for the overall posterior distributions (Fig. 8b). The posterior PDFs are significantly narrower than the prior PDFs, suggesting tighter constraints from the amplitude ratio measurements. In particular, the proportion of the ISO components (ζ^2) is much better resolved and significantly more dominant (∼90%) than the prior distributions (Fig. 9), which strongly suggest explosive source

mechanisms. Meanwhile, diffMT inversions reduce the uncertainties of the moment magnitude differences (average standard deviation error of 0.04 for prior and 0.01 for posterior) (Fig. 8c), and make it much easier to compare the size of these nuclear tests. Therefore, the diffMT results could improve explosion discrimination and size comparison for the studied North Korea nuclear tests.

Moreover, diffMT inversion significantly reduces the uncertainty of the DC component (strike, dip and rake in Fig. 8b). To illustrate the improvement, we compared the DC focal mechanism ensembles for the gCAP prior and diffMT posterior distributions (Fig. 10). The gCAP prior ensemble shows highly scattered strike and dip angles. In contrast, the diffMT focal mechanisms converge well, with strike and dip variances generally less than 40 degrees. The diffMT solutions suggest a similar high angle dip-slip as the tectonic release for the three nuclear tests.

5 DISCUSSION

Our application of the diffMT inversion on the North Korea nuclear tests shows better-resolved moment tensors. Although the gCAP inversion uses absolute body and surface wave amplitudes, it does not capture the patterns of amplitude ratios which provide extra constraints on moment tensors. The gCAP and diffMT solutions fit the regional and teleseismic waveforms almost equally well (Supporting Information Fig. S4), suggesting that the absolute amplitude information can hardly distinguish the two moment tensor solutions. In contrast, our final diffMT solution, which is sampled near the mean of the posterior distributions, fits amplitude ratios significantly better than the gCAP solution (Fig. 7). This is because the absolute amplitude information contains the unknown path and site effects that cause misfits that translates to model uncertainties assuming a simple velocity model. On the other hand, diffMT does not require highly accurate velocity models, thus finding better MT solutions from the gCAP ensembles.

Relative moment tensor inversions have been developed and implemented in various studies (Dahm 1996; Plourde & Bostock 2019; Voytan *et al.* 2019; Xu *et al.* 2020). Compared with these methods, our diffMT inversion uses a two-step approach to combine the waveforms with the amplitude ratio information, and quantify moment tensor uncertainties in a Bayesian framework, which provides a natural uncertainty analysis. Introducing the Bayesian framework also eliminates the need of choosing reference events, and avoids the magnitude trade-offs with constraints from the priors. Moreover, diffMT includes surface waves, making it suitable for events with sparse local observations. However, our method still introduces certain assumptions which may bring additional model errors. We did not consider depth phases in the *P* wave amplitude ratio modelling. Although the influence of 1-D depth phases appears insignificant (Supporting Information Fig. S5), the impact of depth phase variations due to the 3-D surface topographic reflections are moderate and need further investigations(Rodgers *et al.* 2010; Avants 2014). Besides, the calculations of body wave amplitude ratios rely on take-off angles calculated with a layered model, and the influence of the source side structural heterogeneities on the ray parameters is presumably low but not negligible. Overall, structural heterogeneities may still bias our inversion results, suggesting that full numerical wavefield simulations with more realistic earth models are needed in the future.

We summarized our final diffMT solutions in Table 1. The proportions of the ISO components are all around 90% (Table 1), substantially more dominant than the gCAP estimates of around 50%–70%, or some other solutions of 50%-60% for the North Korea nuclear tests (Ford *et al.* 2009; Vavryčuk & Kim 2014; Cesca *et al.* 2017). Note that surface waves alone cannot discriminate the ISO and vertical-dipping CLVD sources, as their radiation patterns are similar around the edge of focal sphere. However, the *P* waves can cover the central portion of the beach ball, and the strength of the azimuthal-varying *P* amplitude ratios constrains how much they deviate from uniform radiation (ISO source). The moment magnitudes of these three events are 4.31, 4.28 and 4.43, respectively, suggesting similar sizes for the February 2013 and January 2016 tests, followed by the larger September 2016 test. DC components are mostly dip-slip normal faulting events, and the steep dip angles of tectonic release are suggested by various studies in this region (Ford *et al.* 2009; Barth 2014; Cesca *et al.* 2017). The DC orientations are also consistent with Cesca *et al.* (2017). But similar to the bottlenecks of most moment tensor inversion, our diffMT algorithm only resolves point-source moment tensors for events with clear body and surface waves. Therefore, we skipped the 2009 North Korea nuclear test in our study due to the low SNRs (Supporting Information Fig. S6). We also did not include the September 2017 test (*M* 6.3), because it likely involves sequential explosions, tectonic releases and collapses (Xu *et al.* 2020), which introduces wave complexities (Supporting Information Fig. S6) beyond the point-source assumption. Further investigations of time-dependent source parameters are needed for large and complicated nuclear explosions.

The ISO/DC/CLVD decomposition used in this paper, while used extensively in nuclear monitoring (Ford *et al.* 2009; Vavryčuk & Kim 2014; Cesca *et al.* 2017; Chiang *et al.* 2018), is not the only physical interpretation. Following Aki & Richard's classical model, full moment tensor could be viewed as oblique opening of the fault for one of the two non-perpendicular planes (Aki & Richards 2002; Tape & Tape 2013). Also, a moment tensor can be decomposed as a crack tensor plus a DC (CDC), in which the tensile crack direction is perpendicular to the fault plane of shear motion (Tape & Tape 2013; Alvizuri & Tape 2018). These various kinematic expressions of seismic source can lead to different understandings of the physical processes of nuclear tests.

In our current parametrization of the diffMT inversion, we assume Gaussian priors for the source parameters, which may not best represent the moment tensor variety in the parameter space, and encounter wrap-around at the boundaries. In practice, we truncated the Gaussian functions at the boundaries to avoid jumps for strike/dip/rake. Although moderate changes of prior shape will not significantly influence the diffMT inversion, there are better ways to avoid the non-uniformity of the source parameter distributions. For example, Tape & Tape (2013, 2015) formulate five uniformed parameters that can be mapped to an eigenvalue vector and a triple, to represent unique moment tensors. This way leads to even distributions of moment tensors in the parameter space, which could benefit the prior selection for the diffMT in the future.

6 CONCLUSIONS

We developed a diffMT inversion algorithm that resolves moment tensors of clustered seismic event pairs using relative measurements. It starts with a conventional moment tensor inversion for the *a priori* solutions, followed by inversion on amplitude ratio information for the refinements. Application of diffMT on three North Korea nuclear tests between 2013 and 2016 leads to reduced errors of ISO components and DC focal mechanisms. Their moment tensors have

∼90% explosive components, which are more dominant compared with some conventional results of 50%∼60%, providing opportunity for better explosion discrimination. The associated tectonic release components are small but non-trivial high angle dip-slip mechanisms. The seismic moment differences between events are also better resolved, which could improve energy estimation of nuclear tests. With tighter constraints on the DC focal mechanisms, we expect the diffMT method to be applied to various types of seismic events.

ACKNOWLEDGMENTS

ZJ and ZZ thank and commemorate Don Helmberger for his advising and assistance. We thank the Global Seismic Network (GSN), the International Federation of Digital Seismograph Networks (FDSN), the French Global Network (G), and the Japan Meteorological Agency Seismic Network (JP) for collecting the seismic data, and thank the Incorporated Research Institutions for Seismology (IRIS) for providing public access to them. We thank editor Carl Tape, assistant editor Fern Storey, reviewer Alexandre Plourde and two other anonymous reviewers for their valuable comments. We thank Jack Muir for helpful discussions. This work was supported by Air Force Research Laboratory (AFRL) Grant FA9453-18-C-0058.

DATA AVAILABILITY

All the data used in our study can be downloaded from the IRIS Data Management Center (http://ds.iris.edu/wilber3/find_event).

CONFLICT OF INTEREST

The authors declare no conflict of interest recorded.

REFERENCES

Aki, K. & Richards, P.G., 2002. *Quantitative Seismology,* 2nd edn, University Science Books.

Alvizuri, C. & Tape, C., 2018. Full moment tensor analysis of nuclear explosions in North Korea, *Seismol. Res. Lett.,* **89,** 2139–2151.

Avants, M., 2014. Effects of near-source heterogeneity on wave fields emanating from crustal sources observed at regional and teleseismic distances, *PhD thesis*, UC Santa Cruz.

Bai, Q., Ni, S., Chu, R. & Jia, Z., 2020. gCAPjoint, a software package for full moment tensor inversion of moderately strong earthquakes with local and teleseismic waveforms, *Seismol. Res. Lett.,* **91** 3550–3562. , ,

Ballard, S., Hipp, J.R., Begnaud, M.L., Young, C.J., Encarnacao, A.V., Chael, E.P. & Phillips, W.S., 2016. SALSA3D: a tomographic model of compressional wave slowness in the Earth's mantle for improved travel-time prediction and travel-time prediction uncertainty, *Bull. seism. Soc. Am.,* **106,** 2900–2916.

Barth, A., 2014. Significant release of shear energy of the North Korean nuclear test on February 12, 2013, *JSeis,* **18,** 605–615.

Bazargani, F., Hale, D. & Hayes, G.P., 2013. Tensor-guided fitting of subducting slab depths, *Bull. seism. Soc. Am.,* **103,** 2657–2669.

Bozdağ, E., Peter, D., Lefebvre, M., Komatitsch, D., Tromp, J., Hill, J., Podhorszki, N. & Pugmire, D., 2016. Global adjoint tomography: first-generation model, *Geophys. J. Int.,* **207,** 1739–1766.

Cesca, S., Heimann, S., Kriegerowski, M., Saul, J. & Dahm, T., 2017. Moment tensor inversion for nuclear explosions: what can we learn from the 6 January and 9 September 2016 nuclear tests, North Korea?, *Seismol. Res. Lett.,* **88,** 300–310.

Chiang, A., Ichinose, G.A., Dreger, D.S., Ford, S.R., Matzel, E.M., Myers, S.C. & Walter, W., 2018. Moment Tensor source-type analysis for the democratic People's Republic of Korea–declared nuclear explosions (2006–2017) and 3 September 2017 collapse event, *Seismol. Res. Lett.,* **89,** 2152–2165.

Covellone, B.M. & Savage, B., 2012. A quantitative comparison between 1D and 3D source inversion methodologies: application to the Middle East, *Bull. seism. Soc. Am.,* **102,** 2189–2199.

Dahm, T., 1996. Relative moment tensor inversion based on ray theory: theory and synthetic tests, *Geophys. J. Int.,* **124,** 245–257.

Dreger, D., 1994. Empirical Green's function study of the January 17, 1994 Northridge, California earthquake, *Geophys. Res. Lett.,* **21,** 2633–2636.

Duputel, Z., Rivera, L., Kanamori, H. & Hayes, G., 2012. W phase source inversion for moderate to large earthquakes (1990–2010), *Geophys. J. Int.,* **189,** 1125–1147.

Ekström, G., Nettles, M. & Dziewoński, A., 2012. The global CMT project 2004–2010: centroid-moment tensors for 13,017 earthquakes, *Phys. Earth planet. Inter.,* **200,** 1–9.

Fichtner, A., Kennett, B.L., Igel, H. & Bunge, H.-P., 2009. Full seismic waveform tomography for upper-mantle structure in the Australasian region using adjoint methods, *Geophys. J. Int.,* **179,** 1703–1725.

Ford, S.R., Dreger, D.S. & Walter, W.R., 2009. Source analysis of the memorial day explosion, Kimchaek, North Korea, *Geophys. Res. Lett.,* 36.

Ford, S.R., Walter, W.R. & Dreger, D.S., 2012. Event discrimination using regional moment tensors with teleseismic-P constraints, *Bull. seism. Soc. Am.,* **102,** 867–872.

Frohlich, C. & Davis, S.D., 1999. How well constrained are well-constrained T, B, and P axes in moment tensor catalogs?, *J. geophys. Res.,* **104,** 4901–4910.

Hardebeck, J.L. & Hauksson, E., 2001. Crustal stress field in southern California and its implications for fault mechanics, *J. geophys. Res.,* **106,** 21 859–21 882.

Hastings, W.K., 1970. Monte Carlo sampling methods using Markov chains and their applications, *Biometrika,* **57,** 97–109.

Hauksson, E., 1994. State of stress from focal mechanisms before and after the 1992 Landers earthquake sequence, *Bull. seism. Soc. Am.,* **84,** 917–934.

Hayes, G.P., Wald, D.J. & Keranen, K., 2009. Advancing techniques to constrain the geometry of the seismic rupture plane on subduction interfaces a priori: higher-order functional fits, *Geochem. Geophys. Geosyst.,* **10,** Q09006.

Jia, Z., Ni, S., Chu, R. & Zhan, Z., 2017. Joint inversion for earthquake depths using local waveforms and amplitude spectra of Rayleigh waves, *Pure appl. Geophys.,* **174,** 261–277.

Jia, Z., Shen, Z., Zhan, Z., Li, C., Peng, Z. & Gurnis, M., 2020a. The 2018 Fiji M_w 8.2 and 7.9 deep earthquakes: one doublet in two slabs, *Earth planet. Sci. Lett.,* **531,** 115997.

Jia, Z., Wang, X. & Zhan, Z., 2020b. Multifault models of the 2019 ridge-crest sequence highlight complementary slip and fault junction instability, *Geophys. Res. Lett.,* **47,** e2020GL089802.

Kanamori, H. & Rivera, L., 2008. Source inversion of W phase: speeding up seismic tsunami warning, *Geophys. J. Int.,* **175,** 222–238.

Kennett, B.L., Engdahl, E. & Buland, R., 1995. Constraints on seismic velocities in the Earth from traveltimes, *Geophys. J. Int.,* **122,** 108–124.

Kikuchi, M. & Kanamori, H., 1991. Inversion of complex body waves—III, *Bull. seism. Soc. Am.,* **81,** 2335–2350.

Lay, T., Burdick, L. & Helmberger, D.V., 1984. Estimating the yields of the Amchitka tests by waveform intercorrelation, *Geophys. J. Int.,* **78,** 181–207.

Lee, E.J., Chen, P., Jordan, T.H., Maechling, P.B., Denolle, M.A. & Beroza, G.C., 2014. Full-3-D tomography for crustal structure in southern California based on the scattering-integral and the adjoint-wavefield methods, *J. geophys. Res.,* **119,** 6421–6451.

Liu, H., Gurnis, M., Leng, W., Jia, Z. & Zhan, Z., 2021. Tonga slab morphology and stress variations controlled by a relic slab: implications for deep earthquakes in the Tonga-Fiji Region, *Geophys. Res. Lett.,* **48,** e2020GL091331.

Minson, S.E. & Dreger, D.S., 2008. Stable inversions for complete moment tensors, *Geophys. J. Int.,* **174,** 585–592.

Ni, S., Helmberger, D. & Pitarka, A., 2010. Rapid source estimation from global calibrated paths, *Seismol. Res. Lett.,* **81,** 498–504.
Plourde, A.P. & Bostock, M.G., 2019. Relative moment tensors and deep Yakutat seismicity, *Geophys. J. Int.,* **219,** 1447–1462.
Rodgers, A.J., Petersson, N.A. & Sjogreen, B., 2010. Simulation of topographic effects on seismic waves from shallow explosions near the North Korean nuclear test site with emphasis on shear wave generation, *J. geophys. Res.,* **115,** doi:10.1029/2010JB007707.
Savage, B., Morency, C., Covellone, B.M., Rodgers, A. & Tromp, J., 2014. Short-period, anelastic and anisotropic, waveform-based 3D Middle East model to improve nuclear explosion monitoring, RHODE ISLAND UNIV KINGSTON KINGSTON United States.
Simmons, N.A., Myers, S.C., Johannesson, G. & Matzel, E., 2012. LLNL-G3Dv3: global *P* wave tomography model for improved regional and teleseismic travel time prediction, *J. geophys. Res.,* **117,** doi:10.1029/2012JB009525.
Tan, Y. & Helmberger, D., 2007. A new method for determining small earthquake source parameters using short-period P waves, *Bull. seism. Soc. Am.,* **97,** 1176–1195.
Tao, K., Grand, S.P. & Niu, F., 2017. Full-waveform inversion of triplicated data using a normalized-correlation-coefficient-based misfit function, *Geophys. J. Int.,* **210,** 1517–1524.
Tape, C., Liu, Q., Maggi, A. & Tromp, J., 2009. Adjoint tomography of the southern California crust, *Science,* **325,** 988–992.
Tape, W. & Tape, C., 2012. A geometric setting for moment tensors, *Geophys. J. Int.,* **190,** 476–498.
Tape, W. & Tape, C., 2013. The classical model for moment tensors, *Geophys. J. Int.,* **195,** 1701–1720.
Tape, W. & Tape, C., 2015. A uniform parametrization of moment tensors, *Geophys. J. Int.,* **202,** 2074–2081.
Tarantola, A., 2005. *Inverse Problem Theory and Methods for Model Parameter Estimation,* SIAM.
Vallée, M., 2007. Rupture properties of the giant Sumatra earthquake imaged by empirical Green's function analysis, *Bull. seism. Soc. Am.,* **97,** S103–S114.
Vavryčuk, V. & Kim, S.G., 2014. Nonisotropic radiation of the 2013 North Korean nuclear explosion, *Geophys. Res. Lett.,* **41,** 7048–7056.
Voytan, D.P., Lay, T., Chaves, E.J. & Ohman, J.T., 2019. Yield estimates for the six north Korean nuclear tests from teleseismic P wave modeling and intercorrelation of P and Pn recordings, *J. geophys. Res.,* **124,** 4916–4939.
Waldhauser, F. & Ellsworth, W.L., 2000. A double-difference earthquake location algorithm: method and application to the northern Hayward fault, California, *Bull. seism. Soc. Am.,* **90,** 1353–1368.
Wang, D. & Hutko, A.R., 2018. Relative relocations of the North Korean nuclear tests from 2006 to 2017 using the Hi-Net array in Japan, *Geophys. Res. Lett.,* **45,** 7481–7487.
Wang, X. & Zhan, Z., 2020a. Moving from 1-D to 3-D velocity model: automated waveform-based earthquake moment tensor inversion in the Los Angeles region, *Geophys. J. Int.,* **220,** 218–234.
Wang, X. & Zhan, Z., 2020b. Seismotectonics and fault geometries of the 2019 Ridgecrest sequence: insight from aftershock moment tensor catalog using 3-D Green's functions, *J. geophys. Res.,* **125,** e2020JB019577.
Xu, H., Ni, S., Liu, W., Zhu, H. & Wang, X., 2020. Focal mechanisms of the 2017 North Korean nuclear test and its early collapse event, *Geophys. J. Int.,* **220,** 737–752.
Yang, T., Gurnis, M. & Zhan, Z., 2017. Trench motion-controlled slab morphology and stress variations: implications for the isolated 2015 Bonin Islands deep earthquake, *Geophys. Res. Lett.,* **44,** 6641–6650.
Zhan, Z. *et al.*, 2012. Anomalously steep dips of earthquakes in the 2011 Tohoku-Oki source region and possible explanations, *Earth planet. Sci. Lett.,* **353,** 121–133.
Zhang, M. & Wen, L., 2013. High-precision location and yield of North Korea's 2013 nuclear test, *Geophys. Res. Lett.,* **40,** 2941–2946.
Zhang, M. & Wen, L., 2015. Seismological evidence for a low-yield nuclear test on 12 May 2010 in North Korea, *Seismol. Res. Lett.,* **86,** 138–145.
Zhao, L.S. & Helmberger, D.V., 1994. Source estimation from broad-band regional seismograms, *Bull. seism. Soc. Am.,* **84,** 91–104.
Zhu, L. & Ben-Zion, Y., 2013. Parametrization of general seismic potency and moment tensors for source inversion of seismic waveform data, *Geophys. J. Int.,* **194,** 839–843.
Zhu, L. & Helmberger, D.V., 1996. Advancement in source estimation techniques using broadband regional seismograms, *Bull. seism. Soc. Am.,* **86,** 1634–1641.
Zhu, L. & Rivera, L.A., 2002. A note on the dynamic and static displacements from a point source in multilayered media, *Geophys. J. Int.,* **148,** 619–627.

SUPPORTING INFORMATION

Supplementary data are available at *GJI* online.

Figure S1. Distribution of gCAP source parameters from bootstrapping sampling in the synthetic test. Results for E1 and E2 are shown in panels (a) and (b), respectively.
Figure S2. Same as Fig. S1, but for the three studied North Korea nuclear explosions.
Figure S3. Measurement of amplitude ratios among the three studied North Korea nuclear explosions. The symbols are similar to that in Fig. 5(a).
Figure S4. Comparison of waveform fittings for the (a) gCAP and (b) diffMT solutions. The fitting difference is hardly observable, suggesting that the moment tensor difference of these two solutions cannot be resolved by the gCAP waveform inversion.
Figure S5. Influence of 1-D depth phases (pP, sP) on the body wave amplitude ratios for the synthetic events E1 and E2. (a) Comparison of *P*-wave amplitude ratios from waveform cross-correlation (with depth phases; black squares) and analytical calculation (without depth phases; red crosses). The depths used to generate synthetic waveforms are both 0.6 km for E1 and E2. (b) Same as (a), but the depths used to generate synthetic waveforms are 0.6 and 1.2 km for E1 and E2, respectively.
Figure S6. Seismograms of the North Korea nuclear explosions recorded at (a) a regional and (b) a teleseismic station.

Please note: Oxford University Press is not responsible for the content or functionality of any supporting materials supplied by the authors. Any queries (other than missing material) should be directed to the corresponding author for the paper.